THE JOURNAL OF PHYSICAL CHEMISTRY A

pubs.acs.org/JPCA Article

Acoustic Vibrations of Al Nanocrystals: Size, Shape, and Crystallinity Revealed by Single-Particle Transient Extinction Spectroscopy

Published as part of The Journal of Physical Chemistry virtual special issue "Time-Resolved Microscopy".

Behnaz Ostovar, Man-Nung Su, David Renard, Benjamin D. Clark, Pratiksha D. Dongare, Chayan Dutta, Niklas Gross, John E. Sader, Christy F. Landes, Wei-Shun Chang, Naomi J. Halas, and Stephan Link*

Cite This: *J. Phys. Chem. A* 2020, 124, 3924−3934 Read Online

ABSTRACT: Acoustic vibrations in plasmonic nanoparticles, monitored by an all-optical means, have attracted significant increasing interest because they provide unique insight into the mechanical properties of these metallic nanostructures. Al nanostructures are a recently emerging alternative to noble metal nanoparticles, because their broad wavelength tunability and high natural abundance make them ideal for many potential applications. Here, we investigate the acoustic vibrations of individual Al nanocrystals using a combination of electron microscopy and single-particle transient extinction spectroscopy, made possible with a low-pulse energy, high sensitivity, and probe-wavelength-tunable, single-particle transient extinction microscope. For chemically synthesized, faceted Al nanocrystals, the observed vibration frequency scales with the inverse particle diameter. In contrast, triangularly shaped Al nanocrystals support two distinct frequencies, corresponding to their in- and out-of-plane breathing modes. Unlike ensemble measurements, which measure average properties, measuring the damping time of the acoustic vibrations for individual particles enables us to investigate variations of the quality factor on the particle-to-particle level. Surprisingly, we find a large variation in quality factors even for nanocrystals of similar size and shape. This observed heterogeneity appears to result from substantially varying degrees of nanoparticle crystallinity even for chemically synthesized nanocrystals.

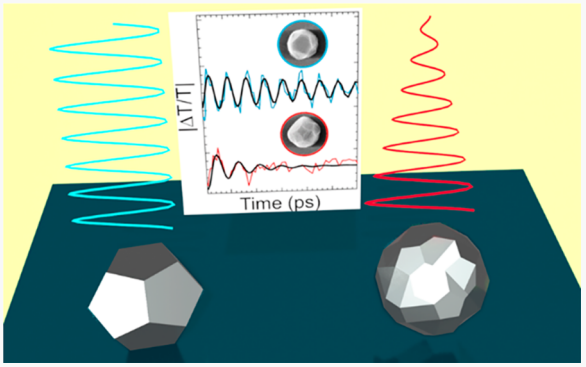

INTRODUCTION

Metallic and semiconducting nanomechanical resonators that support coherent phonon modes in the GHz and THz regimes are receiving increasing attention because of their applications as optomechanical devices,[1−4] biosensors,[5,6] sensitive mass spectrometers,[7,8] and programmable devices.[9,10] Plasmonic nanoparticles are ideal for studying the dynamics of acoustic vibrations because of the unique properties of the localized surface plasmon resonance (LSPR)[11] and because of the large tunability of the acoustic vibration frequency.[12] Ultrafast pump−probe spectroscopy provides a particularly unique way to study the nanomechanical vibrational dynamics of plasmonic nanoparticles. Acoustic vibrations in plasmonic nanoparticles can be launched following excitation with ultrafast laser pulses. Short-pulse excitation first creates a hot electron distribution.[13−17] Strong electron−phonon coupling then leads to heating of the lattice within a few picoseconds, a time scale shorter than the periods of an acoustic breathing mode. Because of this impulsive heating and accompanied lattice expansion, coherent phonon modes are excited, which in turn are probed optically as they induce changes in the LSPR. On longer time scales, the nanoparticles dissipate energy to the environment by means of phonon−phonon coupling.

Both ensemble and single-particle approaches have provided detailed insight into the acoustic breathing modes of plasmonic nanoparticles, and comparison with theory has yielded their corresponding nanomechanical properties.[18−24] Single-particle transient extinction spectroscopy is advantageous over ensemble measurements: by eliminating sample size and shape heterogeneity, the dependence of the vibrational dynamics on size, shape, material, and surrounding environment of the nanoparticles can be accurately determined.[25] In particular, due to the strong size dependence of the vibration frequency, only single-particle methods are capable of

Received: February 11, 2020
Revised: April 8, 2020
Published: April 14, 2020

https://dx.doi.org/10.1021/acs.jpca.0c01190
J. Phys. Chem. A 2020, 124, 3924−3934

unequivocally measuring the intrinsic damping time of coherent oscillations.

Despite the advantages of nanomechanical resonators that are excited and detected all-optically, one of the important limiting factors for applications is their limited lifetime, resulting in low quality factors (Q-factors).[26,27] Extending the lifetime of the vibrational mode in Au and Ag nanostructures has been reported by engineering the nanoparticle shape to achieve mode hybridization through substrate isolation,[28] reducing losses using unsupported thin films,[29] suspending nanostructures over trenches,[30] and improving nanoparticle crystallinity.[26,31,32] Comparing colloidal Au nanoparticles to lithographically prepared nanostructures with precise dimensions and hence well-controlled vibration frequencies, it has been demonstrated that the Q-factor of monocrystalline nanostructures prepared by chemical synthesis is up to 3 times larger.[26,31] For a variety of polycrystalline Au nanoparticles fabricated by electron-beam lithography, an almost universal Q-factor of about 11.3 ± 2.5 was found and assigned to the damping of acoustic vibrations by lattice defects.[26] However, it is not known if the effect of polycrystallinity on the damping of acoustic vibrations is as readily observable in other metals.

Because of their highly tunable LSPRs and natural abundance, Al nanostructures have emerged as an alternative to noble metals.[33−41] While some recent studies have explored the ultrafast properties of Al nanostructures,[33,36,37,42] the effect of crystallinity on the acoustic vibrations has not yet been investigated. Here, we applied single-particle transient extinction spectroscopy together with correlated scanning electron microscopy (SEM) to determine the acoustic vibration frequencies and intrinsic damping times of colloidal Al nanocrystals (AlNCs) of various sizes and shapes. The resulting Q-factors were found to be independent of size for quasi-spherical AlNCs but varied significantly from particle to particle. We ascribe this heterogeneity to different degrees of particle crystallinity, as further elaborated by electron microscopy and comparison to Q-factors measured for polycrystalline, lithographically fabricated Al nanodisks (AlNDs).

METHODS

Synthesis of Colloidal AlNC Samples. AlNCs prepared by colloidal wet chemical synthesis were selected from three chemically synthesized samples with average sizes of 133 ± 15, 157 ± 19, and 172 ± 23 nm. Larger sizes were studied to shift the LSPR into the visible spectral range.[39] These colloidal AlNCs were synthesized via titanium(IV)-catalyzed decomposition of dimethylethylamine alane (DMEAA), as previously reported.[43] Briefly, volume mixtures of tetrahydrofuran (THF) and 1,4-dioxane totaling 24 mL were heated to 40 °C while vigorously stirring in a Schlenk flask under an argon atmosphere. Different THF volume fractions were used to obtain particles with different sizes. Then, 6 mL of 0.5 M DMEAA in toluene was added via a syringe and allowed to heat to 40 °C, followed by addition of 1.5 mL of 50 mM titanium(IV) isopropoxide in toluene. The colorless solutions immediately turned brown and gradually became opaque gray over the course of 4 h, indicating the formation of AlNCs. The reaction was then cooled to room temperature and 10 mL 50 mM dibutylphosphate in cyclohexane was added to cap the particle surface and remove unreacted DMEAA. Finally, the AlNCs were collected via centrifugation and washed several times in isopropyl alcohol (IPA).

The AlNCs were imaged using a JEOL 1230 HC transmission electron microscope (TEM) operating at 80 kV by drop-casting a diluted sample onto a carbon-coated copper TEM grid (Ted Pella). Figure S1 shows a representative TEM image, illustrating the different particle shapes encountered: truncated octahedron, singly twinned Wulff construction, truncated triangular plate, and multiply twinned crystal, in agreement with previous studies.[44] The average sizes were determined by measuring the long-axis diameters of all nanoparticles from multiple TEM images for all three samples using the software ImageJ.

Indexed glass substrates were employed for the single-particle measurements. A dilute base piranha solution (1:4:20 $NH_4OH/H_2O_2/H_2O$) was used for cleaning the glass substrates (Corning). After rinsing with Millipore deionized water, the glass substrates were dried using a stream of N_2 gas. A TEM grid shadow mask was used to create indexed patterns on the glass substrates by evaporating 35 nm of Au and then removing the mask. The indexed patterns allowed for single-particle measurements to be correlated with SEM images of the same particle. The indexed glass substrates were then O_2 plasma-cleaned for 2 min. The colloidal AlNCs were first diluted and then spin-coated on the indexed glass substrates for 60 s at 2500 rpm to achieve single-particle coverage. Correlated SEM images of AlNCs were obtained after all optical measurements to determine shapes and sizes of the individual AlNCs. The 49 single AlNCs used in this study had shapes of either truncated octahedron or singly twinned Wulff construction. For simplicity, we refer to both of them as quasi-spherical throughout the manuscript. The dimension of each quasi-spherical AlNC was determined by averaging the diameters along its long and short axes. We also measured 9 truncated triangular plates with equilateral edges, labeled as triangular-shaped AlNCs below. As the thickness of triangular-shaped AlNCs could not be determined from 2D SEM images, tilted SEM imaging was conducted on a few AlNCs to determine their thickness. All SEM imaging was performed using a FEI QUANTA 400 ESEM FEG in low-vacuum mode operating at a voltage of 30 kV with a resolution of about 1.5 nm.

Lithography of AlND Samples. The same glass substrates were used for AlND fabrication using electron-beam lithography.[36] First, the glass substrates were sonicated for 5 min in acetone and 5 min in IPA, followed by argon (75%)/oxygen (25%) plasma cleaning for 2 min. A poly(methyl methacrylate) resist (PMMA 950 A2, MicroChem) and the conductive polymer Espacer 300Z (Showa Denko) were then spin-coated on the cleaned glass substrates. The resist was patterned with an electron beam using a FEI QUANTA 650 SEM at a beam current of 40 pA and an operating voltage of 30 kV. Development was carried out in a 1:3 methyl isobutyl ketone (MIBK):IPA solution and Al was then evaporated at a pressure of 10^{-7} Torr. The film thickness was monitored with a quartz crystal microbalance. Finally, lift-off was achieved by immersing the sample in *N*-methy-2-pyrrolidone at 65 °C for 10 h. The diameters of the lithographically fabricated AlNDs ranged from 170, 210, 250, 290, to 350 nm. Au nanodisks were prepared similarly as described in ref 26.

Single-Particle Transient Extinction Spectroscopy. Transient extinction spectroscopy was performed on a home-built instrument by incorporating a pump−probe setup into a

https://dx.doi.org/10.1021/acs.jpca.0c01190
J. Phys. Chem. A 2020, 124, 3924−3934

single-particle microscope (Zeiss Axio Observer.D1m).[20] A 532 nm laser (Coherent Verdi) pumped a Ti-Sapphire oscillator (KMLab Griffin), producing sub-100 fs pulses at a center wavelength at 828 nm with an average output power of 544 mW at 86 MHz (Figure S2). Here, 25% of the fundamental beam was used as the pump, either directly or after frequency-doubling in a beta barium borate (BBO) crystal (Altos BBO-1004H), while 70% was sent into a nonlinear photonic crystal fiber (FemtoWHITE 800) for generation of a white light continuum. The white light continuum served as the probe beam after selecting a 25 nm spectral slice with various bandpass filters. Also, 5% of the fundamental beam was aligned as an alternative probe beam, allowing us to determine the stability of the white light continuum under the same pump−probe conditions. The probe beam was passed through an optical delay line (Newport UTS150CC), while the pump beam was modulated with a chopper (Newport 3502) at a frequency of 10 kHz. The pump and probe beams were recombined using a dichroic mirror and focused on the sample with either a 63× refractive objective with a numerical aperture (N.A.) of 1.4 (Zeiss Plan-Apochromat) or a reflective objective (Ealing, 36×, N.A. = 0.5). The collinear pump and probe beams were collected after the sample by a 40× objective with a N.A. of 0.6 (Zeiss LD Achroplan) in a transmission geometry. The probe beam then passed through an 800 nm short-pass filter to remove the pump beam and was detected by a photodiode that was connected to a lock-in amplifier synchronized to the frequency of the optical chopper. The change in transmission ΔT, induced by the pump beam and read out by the lock-in amplifier, was then digitized using a data acquisition board (National Instruments). The transmission T without pump was recorded with an oscilloscope and used to express all signals as $\Delta T/T$.

Transient transmission images were acquired by moving the sample with a piezo scanning stage (Physik Instrumente P-517.3CL) and were used to locate individual nanoparticles. Pump and probe beams were temporally overlapped when acquiring images. Transient transmission decays were acquired by first positioning an individual nanoparticle over the pump and probe beams and then scanning the optical delay line. Each pump−probe measurement was repeated at least two times to ensure the stability of the optical setup and to eliminate the possibility of laser-induced thermal reshaping of the nanoparticles under the excitation powers used (Figure S3). The instrument response function (IRF) was determined by cross-correlation of the pump and probe beams in a BBO crystal (Altos BBO-1004H) mounted at the sample position on the microscope. Pump and probe power densities and wavelengths are specified in the figure captions. The power density was calculated by measuring the beam power after the objective and its size as determined based on the knife-edge method.[45,46] Pump and probe beam sizes of 1000 and 1300 nm (expressed as the full width at half-maximum (fwhm)) were determined in this way for the reflective objective, while the corresponding values for the refractive objective were 500 and 600 nm.

RESULTS AND DISCUSSION

Investigating individual nanoparticles eliminates inhomogeneous broadening in measurements of their physical properties. Imaging and spectroscopy of single plasmonic nanoparticles can be routinely achieved using dark-field excitation in a microscope using a low power lamp.[47−52] Ultrafast optical spectroscopy with femtosecond laser pulses, however, requires a refined balance between low-power excitation pulses to avoid photodamage of the sample, high repetition rates to average the resulting smaller signals, and spectral tunability for pumping and probing various transitions. To realize a versatile, wavelength tunable ultrafast transient extinction microscope with diffraction limited optical resolution we have combined an unamplified Ti:sapphire oscillator operating at a repetition rate of 86 MHz with a nonlinear photonic crystal fiber (Figure 1A, see the Methods section for more details) to generate wavelength tunable pulses from 500 to 950 nm (Figure 1B),

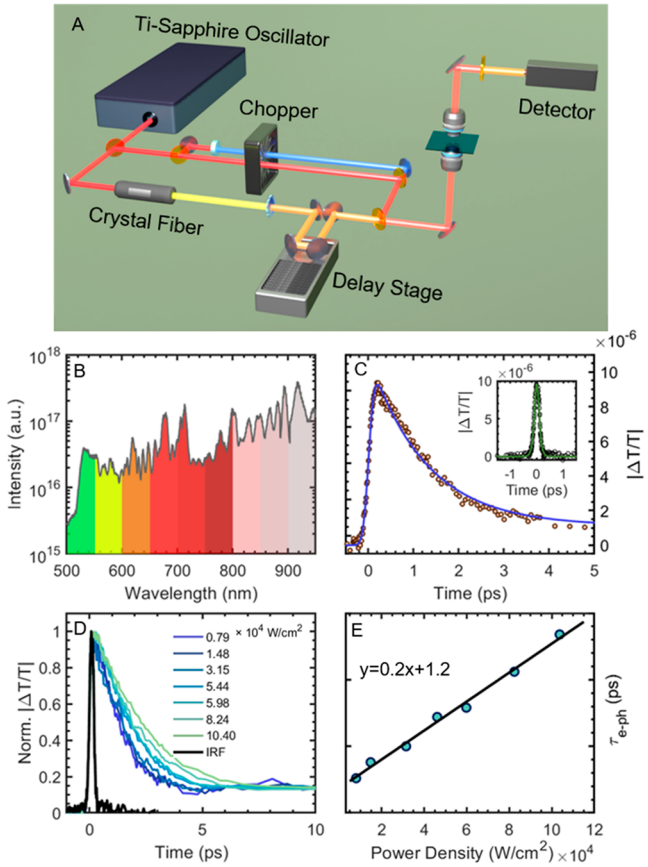

Figure 1. (A) Schematic illustration of the transient extinction setup. (B) Spectrum of the white light continuum generated by the photonic crystal fiber, collected by an Ocean Optics USB4000 spectrometer. The wavelength dependent detection efficiency of the spectrometer was corrected using a calibration lamp (Ocean Optics LS-1 Cal). The colored spectral slices indicate the different probe wavelengths that can be used, i.e. from 500 to 950 nm in 50 nm steps. (C) Transient transmission of a single Au nanodisk having a diameter of 160 nm and height of 35 nm after excitation with the fundamental laser wavelength and probed at 700 nm (red dots). (inset) Corresponding IRF (black dots) determined for the pump and probe beams with the green line showing a fit to a $\text{sech}^2\ x$ function yielding a fwhm of 250 fs. Using this value as the instrument time resolution, the transient transmission of the Au nanodisk was fit to a convolution of a Gaussian IRF and two exponential decays (blue line, eq 1). The pump and probe power densities were 7.90×10^3 and 4.84×10^2 W/cm^2, respectively. (D) Normalized transient transmissions of a 160 nm Au nanodisk as a function of pump power density as indicated in the legend. The IRF (black line) is given for comparison. (E) Electron−phonon relaxation times $\tau_{\text{e-ph}}$ (blue circles) extracted from the transient transmissions using eq 1 as a function of pump power density. The black line is the linear regression of the data.

https://dx.doi.org/10.1021/acs.jpca.0c01190
J. Phys. Chem. A 2020, 124, 3924−3934

as also described in previous work.[36] Without pulse compression or pulse shaping, the choice of objective determines both the spatial and temporal resolution of this approach. Using a lower N.A. reflective objective, we achieved a temporal resolution of ∼250 fs (Figure 1C, inset) with a spatial resolution of 1150 nm for a nanoparticle with subdiffraction dimensions (Figure S4). Conversely, the spatial resolution could be reduced to 350 nm for the same 160 nm diameter Au nanodisk using a higher N.A. refractive objective at the cost of a reduced temporal resolution of 400 fs (Figure S4). Based on the transient transmission for the Au nanodisk shown in Figure 1C measured at the lowest power density of the pump beam, we recorded a differential transmission change $\Delta T/T$ of 10^{-5} with a signal-to-noise ratio of 40. We therefore can easily achieve values of 10^{-6} and likely even lower for extended signal averaging times.

In a set of initial measurements using this approach, we measured the electron−phonon relaxation time of Au nanoparticles as a function of pump beam power. From ensemble studies it is well-known that the measured lifetime of the optically induced transient bleaching of the plasmon resonance in Au nanoparticles is dependent on the initial electron temperature. Only by using very low excitation powers,[53−55] or by extrapolating to zero pump power, can the true electron−phonon relaxation time $\tau_{e\text{-}ph}$ be obtained, e.g. ∼1 ps for Au.[56,57] Low pulse energies, high detection sensitivity, and subpicosecond time resolution are all required for this measurement, making Au nanoparticles an ideal test sample for our experimental approach. We recorded the transient transmission of individual 160 nm diameter lithographically prepared Au nanodisks with a LSPR at 730 nm.[26] By selecting 700 nm as the probe pulse wavelength and thereby matching the LSPR of the nanodisks ensured that we probed close to the maximum of the transient bleaching, as illustrated in Figure 1C. The rise and decay of this pump−probe signal can be described by a convolution of a Gaussian IRF with the sum of two exponential decays describing electron−phonon $\tau_{e\text{-}ph}$ and phonon−phonon coupling $\tau_{ph\text{-}ph}$:[36]

$$y(t) = A_1 \exp\left(\frac{\sigma^2}{2\tau_1^2} - \frac{t}{\tau_1}\right)\left(1 - \mathrm{erf}\left(\frac{\sigma^2 - \tau_1 t}{\sqrt{2}\,\sigma\tau_1}\right)\right) + A_2 \exp\left(\frac{\sigma^2}{2\tau_2^2} - \frac{t}{\tau_2}\right)\left(1 - \mathrm{erf}\left(\frac{\sigma^2 - \tau_2 t}{\sqrt{2}\,\sigma\tau_2}\right)\right) \quad (1)$$

Here, σ is the standard deviation in the Gaussian function that describes the IRF with a fwhm of 250 fs, where A_1 and A_1 are the amplitudes and τ_1 and τ_2 are the relaxation times of two exponential decays corresponding to $\tau_{e\text{-}ph}$ and $\tau_{ph\text{-}ph}$, respectively. As illustrated by the blue line in Figure 1C, eq 1 describes the data well, and yields $\tau_{e\text{-}ph}$. When lowering the excitation power, the fast decay time of the transient transmission clearly becomes shorter (Figure 1D) which can be understood within the two-temperature model for electron−phonon scattering.[14,58] Plotting the extracted values for $\tau_{e\text{-}ph}$ as a function of pump power density (Figure 1E) yields the expected linear relationship with an intercept of 1.2 ps. This value yields the electron−phonon coupling time for a single particle, agreeing well with previous ensemble measurements.[14,56,57,59,60] To the best of our knowledge, electron−phonon relaxation times for single particles have to date only been reported for silver nanoparticles.[61] This initial series of measurements establishes the capabilities of our experimental setup for subsequent studies of impulsively launched acoustic breathing modes of colloidal AlNCs.

Three colloidal AlNCs samples were studied by combined single-particle transient extinction microscopy and spectroscopy to measure the frequencies and damping times of their acoustic vibrations, followed by SEM to obtain their corresponding sizes. This approach allowed us to investigate a range of nanoparticle dimensions from 110 to 250 nm. Prior to single-particle spectroscopy, a large-area image was scanned to locate individual AlNCs. Figure 2A shows a characteristic transient extinction image of a 20 μm × 20 μm area for the 157 ± 19 nm AlNC sample. Imaging is the key first step for optical studies of randomly deposited colloidal AlNCs, both to identify particles and also to avoid larger, brighter particle aggregates. Figure S5 shows a typical transient transmission of a single AlNC obtained after it was positioned in the center of the pump and probe beams. The experimental data shows, in addition to coherent oscillations, the initial electron and lattice heating as the rise, and lattice cooling as the decay of the signal following femtosecond laser pulse excitation.[33,36] To isolate only the coherent oscillations corresponding to the excitation of an acoustic vibrational mode, the first term in eq S1 describing lattice cooling was subtracted from the raw data. Examples of transient transmissions showing only the acoustic vibrations obtained in this manner are presented in Figure 2B, for three different AlNCs, chosen to cover a large size range. Importantly, the probe wavelength was chosen to maximize the amplitude of the coherent oscillations, made possible by spectral filtering the generated white light continuum. The frequency ν and damping time τ_{HO} were then obtained via fitting with a damped cosine function (black line, Figure 2B):[14,33]

$$A_{HO}\exp\left(-\frac{t}{\tau_{HO}}\right)\cos(2\pi t\nu - \phi) \quad (2)$$

Here, A_{HO} is the amplitude and ϕ represents a phase factor. Fourier transform analysis was performed as an independent check (insets of Figure 2B). For the AlNCs in Figure 2B with diameters of 125, 161, and 181 nm the frequencies of the coherent oscillations are 39.3, 29.4, and 26.5 GHz, respectively.

With the corresponding AlNC diameters from correlated SEM images (insets of Figure 2B), the dependence of the vibration frequency on the nanoparticle diameter was determined for the subset of AlNCs with a quasi-spherical shape. Quasi-spherical nanocrystals were selected to align with the continuum elastic model, which predicts that their vibration frequencies are inversely proportional to the particle diameter.[62−64] Plotting the measured vibration frequencies for quasi-spherical colloidal AlNCs as a function of inverse diameter ($1/D$) indeed yields the expected linear dependence (dotted blue line, Figure 2C), confirming the assignment of the coherent oscillations to lattice vibrations of a radial isotropic breathing mode. Compared to calculated vibration frequencies based on the continuum elastic model and using bulk metal elastic properties, the experimental values obtained were systematically smaller. The fundamental breathing mode of a spherical nanoparticle,[62−64] given by $\nu_{br} = \frac{c_l \chi_n}{\pi D}$, can be computed using the longitudinal speed of sound c_l (equal to 6216 m/s for Al)[65] and a value of 2.79 for χ_n, the lowest order isotropic breathing mode in Al. The calculated trend is shown as the dashed black line in Figure 2C. If we instead fit the data to obtain an effective longitudinal speed of sound, we achieve

https://dx.doi.org/10.1021/acs.jpca.0c01190
J. Phys. Chem. A 2020, 124, 3924−3934

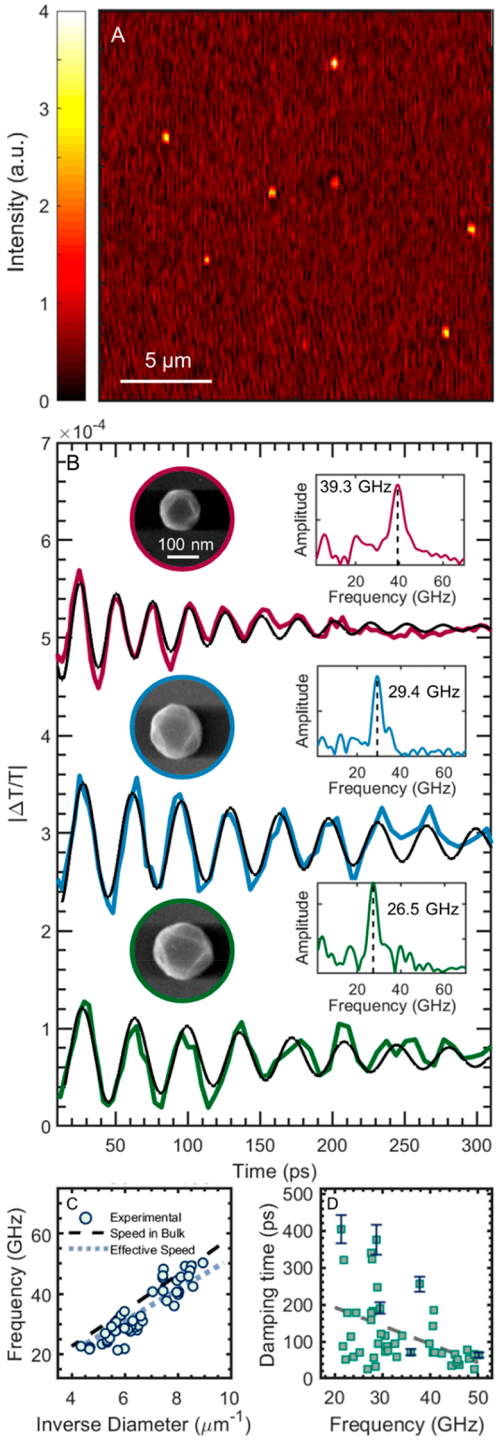

Figure 2. (A) Representative transient extinction image of colloidal AlNCs used to locate individual particles. (B) Representative transient transmissions showing only the acoustic vibrations for single colloidal AlNCs with diameters of 125 (red), 161 (blue), and 181 nm (green). Data are offset for better comparison. The fundamental laser wavelength was used for excitation and a probe wavelength of 650 nm was chosen close to the LSPR maximum in order to maximize the amplitude of the acoustic vibrations. The pump and probe power densities were 8.56×10^4 and 1.41×10^4 W/cm^2, respectively. The black lines indicate fits to the data using a damped cosine function (eq 2), yielding vibration frequencies and damping times. Corresponding normalized Fourier transforms and correlated SEM images of each AlNC are shown as insets. The wings in the Fourier transforms are due to the limited sampling time. (C) Acoustic vibration frequencies of 49 measured AlNCs with a quasi-spherical shape as a function of their inverse diameter as determined by SEM (dark blue circles). The dashed black line shows the expected trend based on an analytical model for spheres using the published longitudinal speed of sound obtained from bulk Al. The dotted blue line is a fit yielding an effective speed of sound for these quasi-spherical AlNCs. The uncertainties in AlNC diameters as estimated based on the resolution of the SEM and uncertainties in the measured frequencies obtained from the fit of the data to eq 2 are comparable to the size of the symbols representing the individual data points. (D) Damping times of all measured AlNCs as a function of vibration frequency. The dashed gray line indicates a linear regression and is shown as a guide only to illustrate an overall decrease in damping time with increasing frequency. Error bars for the measured damping times represent the uncertainties obtained from the fit of the data to eq 2. Only a few representative error bars are shown.

better agreement for a value of 5714 m/s, as indicated by the dotted blue line, consistent with reported smaller elastic moduli for Au nanorods produced by seed-mediated growth compared to bulk Au.[66] The stiffer oxide layer increases the vibration frequency,[33] but the effect is expected to be small considering its small thickness of ∼3 nm in light of previous studies of core−shell nanoparticles.[67] Other factors such as binding to the substrate and different crystallinities within the nanoparticles have been shown to have a minimal effect on the frequencies of the acoustic vibrations[26,68,69] and therefore are likely not important here.

The damping times of the acoustic vibration for 49 quasi-spherical AlNCs in general decreased with larger frequencies or smaller diameters (Figure 2D). However, unlike the vibration frequencies, the damping times showed a large variability as a function of AlNC size. This result emphasizes the advantage of single-particle measurements over ensemble measurements. For ensemble measurements, only average values can be measured, not distributions, and damping times are therefore inherently shortened simply due to averaging (Figure S6). Single-particle studies allow us to measure the actual distribution of damping times for many individual particles, as also further illustrated in Supplementary Movie 1, which shows the out-of-phase intensity oscillations of different AlNCs as a function of probe delay time.

To better understand the origin of the sizable heterogeneity of damping times among the individual nanoparticles, we evaluated the experimental Q-factors, defined as $\pi\nu\tau_{HO}$, which remove the size dependence of the damping time and the acoustic vibration frequency.[25,26,53,70] As illustrated in Figure 3A, the Q-factor has an average value of 11.4, with a large standard deviation of 7.1. In fact, Q-factors for these quasi-spherical colloidal AlNCs vary over an order of magnitude from 3 to 35. By selecting two AlNCs with nearly identical diameters but very different Q-factors and taking advantage of correlated SEM images, we are able to investigate if the observed variation is due to structural differences between the individual nanoparticles. Acoustic vibrations for two quasi-spherical colloidal AlNCs with diameters of 161 and 167 nm are compared in Figure 3B. Their Q-factors are 33.8 (blue, Figure 3B) and 3.0 (red, Figure 3B). As their vibration frequencies with 28.7 and 28.8 GHz are similar, the difference in their Q-factors is a result of very different damping times. Inspection of the correlated SEM images of these two AlNCs (insets of Figure 3B) strongly suggests that they differ in their

https://dx.doi.org/10.1021/acs.jpca.0c01190
J. Phys. Chem. A 2020, 124, 3924−3934

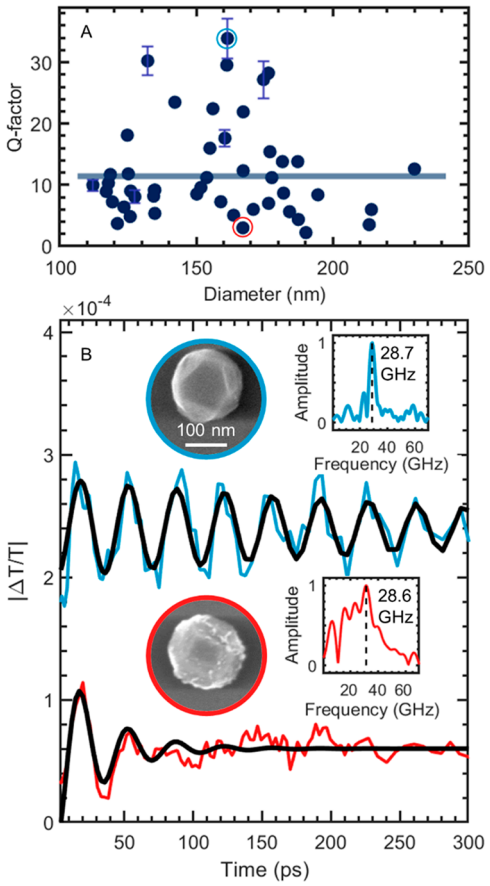

Figure 3. (A) Q-factors of all 49 quasi-spherical AlNCs as a function of their diameter. The blue line represents the average Q-factor of 11.4. Errors for the Q-factors were obtained through error propagation from the measured frequencies and damping times. Only a few representative error bars are shown. (B) Acoustic vibrations for the two colloidal AlNCs marked in panel A. These two AlNCs have similar diameters of 161 (blue) and 167 nm (red). Data are offset for better comparison and were fitted to eq 2 (black line). Corresponding normalized Fourier transforms and correlated SEM images of each AlNC are shown as insets. The pump and probe power densities were 8.56×10^4 and 1.41×10^4 W/cm^2, respectively.

degree of crystallinity: clear and smooth {111} facets, attributed to monocrystalline structures, are observed for the AlNC with the higher Q-factor. Other examples comparing the SEM images of AlNCs with high and low Q-factors are provided in Figure S7. Although these SEM images only indicate surface properties, they lead us to hypothesize whether AlNCs with smooth surfaces have fewer internal defects as well. Closer inspection of the SEM images reveals that the higher Q-factor nanocrystals are truncated octahedra, known to be single crystalline, while the lower Q-factor nanocrystals have the shapes of a singly twinned Wulff construction or a Marks decahedron, which have one or five twin planes, respectively.[44,71,72] Furthermore, TEM diffraction analysis of AlNCs with shapes of a truncated octahedron and a singly twinned Wulff construction confirm the absence and presence of a twin plane (Figure S8). We therefore assign the large heterogeneity in Q-factors to differences in the internal crystallinity among the AlNCs found in the chemically synthesized samples.

We investigated the possible effects of crystallinity on the damping mechanism of the LSPR by studying the line width of correlated single-particle scattering spectra of the two AlNCs shown in Figure 3. The LSPR line widths of these two AlNCs are similar (Figure S9) indicating that plasmon dephasing due to electron scattering at grain boundaries cannot be resolved using scattering spectroscopy for these large nanoparticles. Although polycrystalline nanostructures have been shown to possess larger LSPR line widths due to additional plasmon damping compared to monocrystalline, chemically synthesized nanoparticles,[73,74] the lack of a dependence seen here can be rationalized when considering that for nanoparticles larger than 20−30 nm in diameter, radiation damping is the dominant plasmon decay mechanism and overshadows other damping processes.[47,48,52,75]

The role of crystallinity was confirmed by comparing the acoustic vibrations of colloidal AlNCs to lithographically fabricated AlNDs of similar size. Transient transmissions in Figure 4A show the acoustic vibrations of a 181 nm diameter

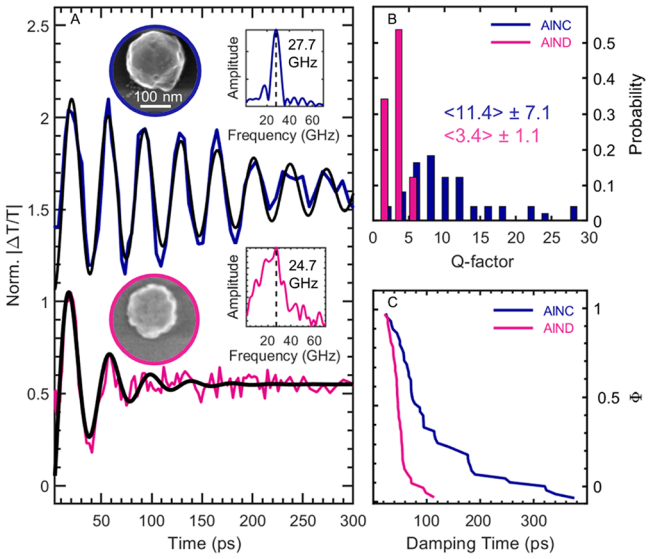

Figure 4. (A) Acoustic vibrations for a single quasi-spherical colloidal AlNC (dark blue) with a diameter of 181 nm compared to a lithographically fabricated AlND (pink) with a diameter of 180 nm and height of 35 nm. The AlND was pumped at the fundamental laser wavelength (power density of 7.52×10^4 W/cm^2) and probed at 650 nm (power density of 1.41×10^4 W/cm^2). Data are offset for better comparison and were fitted to eq 2 (black line). Corresponding normalized Fourier transforms and correlated SEM images of each AlNC are shown as insets. The narrower Fourier transform spectrum of the AlNC compared to the AlND accounts for the associated longer damping time.[31] (B) Histograms of Q-factors for 49 quasi-spherical colloidal AlNCs (dark blue) and 41 lithographically fabricated AlNDs (pink). (C) Complementary cumulative distributions of the corresponding damping times for the nanoparticles shown in panel B. Φ illustrates the fraction of nanoparticles with a value larger than the one indicated by the *x*-axis. The data for the lithographically fabricated AlNDs was previously reported in ref 33.

quasi-spherical colloidal AlNC compared with a 180 nm diameter lithographically fabricated AlND of 35 nm height. Their vibration frequencies were determined to be 27.7 and 24.7 GHz, respectively. Considering the different modes for a spherical nanoparticle and a flat nanodisk, i.e. isotropic radial vs in-plane breathing modes, the experimental frequencies are in quite reasonable agreement. The corresponding Q-factors, however, are markedly different: 15.4 for the AlNC and 2.8 for the AlND, indicating that colloidal AlNCs support a larger Q-

https://dx.doi.org/10.1021/acs.jpca.0c01190
J. Phys. Chem. A 2020, 124, 3924−3934

factor due to a longer damping time than lithographically fabricated AlNDs. This conclusion, derived from only these two examples, is further supported when all measured Q-factors and damping times, irrespective of AlNC or AlND dimensions, are compared (Figure 4B, C). From the distribution of Q-factors for colloidal AlNCs (blue) and lithographically fabricated AlNDs (pink), average Q-factors of 11.4 ± 7.1 and 3.4 ± 1.1 were obtained, reflecting the corresponding magnitude and variation of damping times (Figure 4C).

The increased damping of coherent phonon oscillations for polycrystalline nanostructures fabricated by means of metal evaporation has been well established for several plasmonic metals. It has been assigned to increased phonon scattering at internal crystal defects, rather than surface roughness or binding to the substrate.[26,31,33] For the colloidal AlNCs measured here, their Q-factors can be enhanced by an order of magnitude due to decreased acoustic mode damping. A higher degree of crystallinity is likely made possible by the relatively slow crystal growth in the solution-phase synthesis. However, based on the overlap of Q-factors at low values for both AlNCs and AlNDs (Figure 4B and Figure S10), we also conclude that within the distribution of colloidal AlNCs some nanostructures must have significant internal defects, similar to the AlNDs. The internal defects that occur during growth may result from the complex nucleation and growth process for the AlNCs studied here, which consists of titanium(IV) isopropoxide-catalyzed decomposition of AlH_3 in Lewis base solvents.[76] In this process, both Ti^{3+} and atomic hydrogen are available for accommodation within the growing nanocrystal and may be responsible for nucleating grain boundaries, resulting in the large variations in crystallinity observed in this study.

It has been observed that lithographically prepared Au nanostructures have an almost universal Q-factor independent of size, shape, and substrate because of internal defect scattering becoming the dominant phonon relaxation mechanism.[26] The question therefore arises if Al behaves similarly. The average Q-factor for all lithographically fabricated Au nanostructures was found to be 11.3 ± 2.5.[26] Figure 4B shows the distribution of Q-factors from AlNDs with diameters ranging from 170 to 350 nm, yielding an average Q-factor of 3.4 ± 1.1, lower by about three times compared to Au. However, to compare the mechanical properties between the two metals, the values of their Young's modulus E and density ρ must be considered. For a general damped harmonic oscillator, the Q-factor is given by $k/(\omega b)$, where k is the oscillator stiffness, ω is the angular resonant frequency and b the damping coefficient. The frequency of the in-plane breathing mode can be written as $\omega \propto \sqrt{\frac{E}{\rho}}$,[77] showing that for the same damping coefficient and stiffness, the Q-factor varies as the inverse square root of the density. When correcting the stiffness for the small effect due to Young's modulus (70 GPa for Al and 79 GPa for Au) and the Q-factor for the dominant effect from the density difference (2.7 g/cm^3 for Al and 19.3 g/cm^3 for Al), the average Q-factor for the AlNDs becomes 9.5 ± 3.0, in excellent agreement with the value for Au. This result suggests that there might be a universal, limiting Q-factor for all polycrystalline metallic nanostructures prepared by lithographic methods on a substrate and otherwise surrounded by air. It is worth noting that the acoustic vibrations of lithographically prepared Au nanostructures were damped when the sample was immersed in a liquid environment.[26]

Since the colloidal solutions of AlNCs did not only contain quasi-spherical nanoparticles of various sizes but also different shapes, we also analyzed the effect of geometry. We found that the breaking of spherical symmetry gives rise to an additional acoustic vibration mode in triangular-shaped AlNCs with a spinel twin plane. While the observation of geometric effects in ensemble measurements requires a strict control over size and shape, single-particle measurements with correlated SEM are ideal for the study of heterogeneous samples, making it possible to thoroughly investigate many different nanostructural geometries within just one prepared sample. Figure 5 contrasts the acoustic vibrations for two quasi-spherical

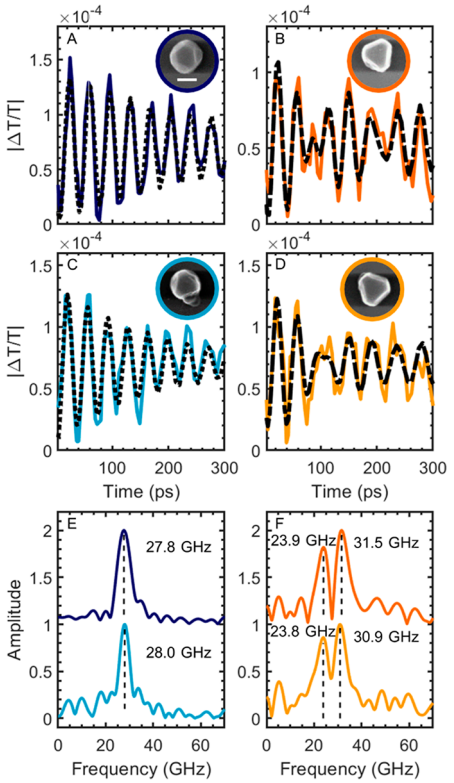

Figure 5. Acoustic vibrations of single quasi-spherical colloidal AlNCs with diameters of 172 (A) and 165 nm (C) compared to single triangular-shaped colloidal AlNCs with edge lengths of 164 (B) and 161 nm (D). The latter were fitted to two damped cosine functions as described by eq 3. Corresponding SEM images of each colloidal AlNC are shown as insets with the scale bar corresponding to 100 nm. These four nanoparticles were chosen because they have similar sizes. (E, F) Corresponding normalized Fourier transforms, offset for better comparison. The pump and probe power densities were 8.56 × 10^4 and 1.41 × 10^4 W/cm^2, respectively.

AlNCs to two triangular-shaped AlNCs with similar sizes. As discussed above, a single acoustic vibration mode is seen for the quasi-spherical AlNCs (Figure 5A, C). The triangular-shaped AlNCs (Figure 5B, D) give rise to more complicated acoustic vibrations where a clear beating can be observed, indicating the excitation of more than one mode. This behavior was the same for the coherent oscillations of all 9 triangular-shaped AlNCs investigated and not found for any of the 49 quasi-spherical AlNCs. If the coherent oscillations for the triangular-shaped AlNCs are modeled with a single damped

https://dx.doi.org/10.1021/acs.jpca.0c01190
J. Phys. Chem. A 2020, 124, 3924−3934

harmonic function, the fit is poor (Figure S11). Much better agreement was achieved when using two damped harmonic oscillations (dashed black lines, Figure 5B, D) according to

$$A_{br1}\exp\left(-\frac{t}{\tau_{br1}}\right)\cos(2\pi t\nu_{br1}-\phi_{br1}) + A_{br2}\exp\left(-\frac{t}{\tau_{br2}}\right)\cos(2\pi t\nu_{br2}-\phi_{br2}) \quad (3)$$

Here A_{br1} and A_{br2} are the amplitudes, τ_{br1} and τ_{br2} are the damping times, ν_{br1} and ν_{br2} are the frequencies, and ϕ_{br1} and ϕ_{br2} are the phases of the two damped harmonic oscillators. Figure S12 shows the details of the fitting using eq 3 for an exemplary triangular-shaped AlNC. The two modes correspond to the in-plane and out-of-plane breathing modes, as further verified below and also consistent with previous studies for Au and Ag nanostructures.[21,29,78,79]

Fourier transform analysis confirms the existence of the additional mode in the acoustic vibrations of triangular-shaped colloidal AlNCs. Quasi-spherical colloidal AlNCs with diameters of 172 nm (dark blue, Figure 5E) and 165 nm (light blue, Figure 5E) possess only one breathing mode at 27.8 and 28 GHz, respectively. Fourier transform analysis for two triangular-shaped colloidal AlNCs with edge lengths of 164 (dark orange, Figure 5F) and 161 nm (light orange, Figure 5F) shows the in-plane and out-of-plane breathing modes with similar amplitudes at 23.9 and 31.5 GHz (dark orange, Figure 5F) and 23.8 and 30.9 GHz (light orange, Figure 5F), respectively. With the measured damping times, we obtain average Q-factors for the 9 triangular-shaped AlNCs of 92.6 ± 18.7 and 11.0 ± 1.9 for the in-plane and out-of-plane vibrations, respectively. These triangular shaped particles are known to have a single twin plane running parallel to the flat face in the particle's center,[44,72] explaining the difference in Q-factors since the out-of-plane acoustic vibration has to travel through this defect while the in-plane mode does not. This result is consistent with our discussion above regarding the crystallinity dominating the damping of acoustic vibrations in colloidal nanoparticles. Furthermore, the remarkably large Q-factor for the in-plane vibration suggests that the triangular-shaped AlNCs are superior from a nanomechanical sensing perspective, warranting further ultrafast studies and the quest for a shape selective synthesis methods.

Using the transient extinction data and, in particular, the extracted vibration frequencies, we are able to deduce the thickness of the triangular-shaped colloidal AlNCs (the SEM images only provide a 2D projection). Nonspherical, oblate nanoparticles have two characteristic dimensions: the edge length and thickness. Correlated SEM images (inset of Figure 5B, D) only reveal the edge length. However, the thickness of the triangular-shaped colloidal AlNCs can be found by applying the frequency dependence of the acoustic vibrations on the dimensions of triangular nanoplates.[29,78] Specifically, assuming isotropic expansion $\nu_{br1} = \frac{c_l}{\sqrt{3}L}$ where L is the edge length and $\nu_{br2} = \frac{c_l}{2T}$ where T is the thickness.[29,78,79] The calculated edge length for the triangular-shaped AlNC shown in Figure 5B using the experimental in-plane breathing mode frequency of 23.9 GHz is 145 nm, close to the experimental edge length of 161 nm obtained from the SEM images. For the longitudinal speed of sound c_l we used here the effective value obtained from the quasi-spherical AlNCs in Figure 2C. Following the same procedure for the out-of-plane breathing mode frequency of 31.5 GHz in Figure 5B using the same effective value for c_l, a thickness of 90 nm is found for the triangular-shaped AlNC. Tilted SEM imaging performed on similar triangular-shaped AlNCs confirms this thickness (Figure S13).

Finally, it is interesting to compare the Q-factors measured here for colloidal AlNCs to those of colloidal Au nanoparticles studied extensively before. When scaled to the material properties of Au (see above), the quasi-spherical AlNCs exhibit an average scaled Q-factor of about 32, which is comparable to the value of 33 for the breathing mode of single colloidal Au nanospheres.[80] This value even slightly exceeds the Q-factor of 28 measured for the breathing mode of single colloidal nanorods on a glass support.[81] However, a more striking difference is seen for their respective standard deviations of the Q-factor distributions. For colloidal Au nanorods a ∼15% standard deviation has been reported.[81] This value increases to about 25% for Au nanostructures prepared by electron-beam lithography[26] and 40% for colloidal nanospheres.[80] For the colloidal AlNCs studied here, it is 60% implying that some of the best AlNCs significantly exceed Q-factors of colloidal Au nanoparticles while others perform poorly. Conducting a similar Q-factor scaling for triangular-shaped AlNCs results in an average scaled Q-factor of about 250 for the in-plane breathing mode, surpassing the recently observed value of ∼130 for single triangular-shaped Au nanoparticles.[29]

CONCLUSIONS

In summary, we characterized the acoustic vibrations of colloidal AlNCs of various sizes and shapes using single-particle femtosecond time-resolved pump−probe spectroscopy correlated with SEM imaging. For quasi-spherical AlNCs, the vibration frequency scales with the inverse particle diameter, consistent with continuum elastic modeling. For triangular shaped AlNCs, two frequencies corresponding to the in-plane and out-of-plane breathing modes were observed, with the latter mode yielding the nanoplate thickness. A surprisingly large variation of Q-factors was observed for AlNCs of similar size, which clearly appears to be related to varying degrees of nanoparticle crystallinity. These results were only possible with our low pulse energy, high sensitivity, and probe wavelength tunable single-particle transient extinction microscope. In addition to large heterogeneities in crystallinity deduced from the wide distribution of Q-factors, the precise measurement of frequencies and intrinsic damping times was enabled by tuning the probe wavelength to maximize oscillation amplitudes, enabling accurate data analysis. Our setup, consisting of only a femtosecond oscillator and a photonic crystal fiber, presents a relatively inexpensive alternative to complex and expensive amplified laser systems for ultrafast microscopy.

ASSOCIATED CONTENT

Supporting Information

The Supporting Information is available free of charge at https://pubs.acs.org/doi/10.1021/acs.jpca.0c01190.

TEM image of AlNCs showing the different shapes; laser pulse characterization; temporal and spatial resolution when using reflective and refractive objectives; reproducibility of transient extinction measurements and data

https://dx.doi.org/10.1021/acs.jpca.0c01190
J. Phys. Chem. A 2020, 124, 3924−3934

analysis; averaged transient extinction measurements for three samples; correlated SEM images of single AlNCs possessing high and low Q-factors; TEM images and electron diffraction patterns of AlNCs; dark-field scattering spectra; Q-factor versus damping time for AlNCs and AlNDs; details of the data analysis of the transient extinction obtained from triangular-shaped AlNCs (PDF)

Movie of the coherent oscillations from several single AlNCs illustrating their out-of-phase intensity variations as a function of probe delay time (AVI)

AUTHOR INFORMATION

Corresponding Author

Stephan Link − *Department of Electrical and Computer Engineering, Department of Chemistry, Laboratory for Nanophotonics, and Smalley-Curl Institute, Rice University, Houston, Texas 77005, United States;* orcid.org/0000-0002-4781-930X; Email: slink@rice.edu

Authors

Behnaz Ostovar − *Department of Electrical and Computer Engineering and Laboratory for Nanophotonics, Rice University, Houston, Texas 77005, United States;* orcid.org/0000-0001-6522-1806

Man-Nung Su − *Department of Chemistry and Laboratory for Nanophotonics, Rice University, Houston, Texas 77005, United States;* orcid.org/0000-0003-2570-4285

David Renard − *Department of Chemistry and Laboratory for Nanophotonics, Rice University, Houston, Texas 77005, United States;* orcid.org/0000-0002-1917-679X

Benjamin D. Clark − *Department of Chemistry and Laboratory for Nanophotonics, Rice University, Houston, Texas 77005, United States;* orcid.org/0000-0003-0390-9538

Pratiksha D. Dongare − *Applied Physics Graduate Program and Laboratory for Nanophotonics, Rice University, Houston, Texas 77005, United States;* orcid.org/0000-0003-0224-8109

Chayan Dutta − *Department of Chemistry and Laboratory for Nanophotonics, Rice University, Houston, Texas 77005, United States;* orcid.org/0000-0003-4839-2245

Niklas Gross − *Department of Chemistry and Laboratory for Nanophotonics, Rice University, Houston, Texas 77005, United States*

John E. Sader − *ARC Centre of Excellence in Exciton Science, School of Mathematics and Statistics, The University of Melbourne, Parkville, VIC 3010, Australia;* orcid.org/0000-0002-7096-0627

Christy F. Landes − *Department of Electrical and Computer Engineering, Department of Chemistry, Department of Chemical and Biomolecular Engineering, Laboratory for Nanophotonics, and Smalley-Curl Institute, Rice University, Houston, Texas 77005, United States;* orcid.org/0000-0003-4163-6497

Wei-Shun Chang − *Department of Chemistry and Biochemistry, University of Massachusetts Dartmouth, North Dartmouth, Massachusetts 02747, United States;* orcid.org/0000-0002-0251-4449

Naomi J. Halas − *Department of Electrical and Computer Engineering, Department of Chemistry, Department of Physics and Astronomy, Laboratory for Nanophotonics, and Smalley-Curl Institute, Rice University, Houston, Texas 77005, United States;* orcid.org/0000-0002-8461-8494

Complete contact information is available at: https://pubs.acs.org/10.1021/acs.jpca.0c01190

Notes

The authors declare no competing financial interest.

ACKNOWLEDGMENTS

We acknowledge financial support from the Robert A. Welch Foundation (C-1787 to C.F.L., C-1664 to S.L., and C-1220 to N.J.H.), the Air Force Office of Scientific Research via the Department of Defense Multidisciplinary University Research Initiative, under Award FA9550-15-1-0022 to N.J.H. and S.L., and the National Science Foundation (CHE-1808382 to C.F.L and ECCS-1608917 to S.L.). J.E.S. gratefully acknowledges support from the Australian Research Council Centre of Excellence in Exciton Science (Grant No. CE170100026) and the Australian Research Council Grants Scheme. This work was conducted in part using resources of the Shared Equipment Authority at Rice University.

REFERENCES

(1) Kippenberg, T. J.; Vahala, K. J. Cavity Optomechanics: Back-Action at the Mesoscale. *Science* **2008**, *321*, 1172.

(2) Favero, I.; Karrai, K. Optomechanics of Deformable Optical Cavities. *Nat. Photonics* **2009**, *3*, 201−205.

(3) Weis, S.; Rivière, R.; Deléglise, S.; Gavartin, E.; Arcizet, O.; Schliesser, A.; Kippenberg, T. J. Optomechanically Induced Transparency. *Science* **2010**, *330*, 1520.

(4) Lin, K.-H.; Lai, C.-M.; Pan, C.-C.; Chyi, J.-I.; Shi, J.-W.; Sun, S.-Z.; Chang, C.-F.; Sun, C.-K. Spatial Manipulation of Nanoacoustic Waves with Nanoscale Spot Sizes. *Nat. Nanotechnol.* **2007**, *2*, 704−708.

(5) Knobel, R. G.; Cleland, A. N. Nanometre-Scale Displacement Sensing Using a Single Electron Transistor. *Nature* **2003**, *424*, 291−293.

(6) Arlett, J. L.; Myers, E. B.; Roukes, M. L. Comparative Advantages of Mechanical Biosensors. *Nat. Nanotechnol.* **2011**, *6*, 203−215.

(7) Naik, A. K.; Hanay, M. S.; Hiebert, W. K.; Feng, X. L.; Roukes, M. L. Towards Single-Molecule Nanomechanical Mass Spectrometry. *Nat. Nanotechnol.* **2009**, *4*, 445−450.

(8) Hanay, M. S.; Kelber, S.; Naik, A. K.; Chi, D.; Hentz, S.; Bullard, E. C.; Colinet, E.; Duraffourg, L.; Roukes, M. L. Single-Protein Nanomechanical Mass Spectrometry in Real Time. *Nat. Nanotechnol.* **2012**, *7*, 602−608.

(9) Masmanidis, S. C.; Karabalin, R. B.; De Vlaminck, I.; Borghs, G.; Freeman, M. R.; Roukes, M. L. Multifunctional Nanomechanical Systems Via Tunably Coupled Piezoelectric Actuation. *Science* **2007**, *317*, 780−783.

(10) Mahboob, I.; Yamaguchi, H. Bit Storage and Bit Flip Operations in an Electromechanical Oscillator. *Nat. Nanotechnol.* **2008**, *3*, 275−279.

(11) Kreibig, U.; Vollmer, M. *Optical Properties of Metal Clusters*; Springer: Berlin, 1995.

(12) Maioli, P.; Stoll, T.; Sauceda, H. E.; Valencia, I.; Demessence, A.; Bertorelle, F.; Crut, A.; Vallée, F.; Garzón, I. L.; Cerullo, G.; et al. Mechanical Vibrations of Atomically Defined Metal Clusters: From Nano- to Molecular-Size Oscillators. *Nano Lett.* **2018**, *18*, 6842−6849.

(13) Link, S.; El-Sayed, M. A. Optical Properties and Ultrafast Dynamics of Metallic Nanocrystals. *Annu. Rev. Phys. Chem.* **2003**, *54*, 331−366.

(14) Hartland, G. V. Optical Studies of Dynamics in Noble Metal Nanostructures. *Chem. Rev.* **2011**, *111*, 3858−3887.

(15) Perner, M.; Gresillon, S.; März, J.; von Plessen, G.; Feldmann, J.; Porstendorfer, J.; Berg, K. J.; Berg, G. Observation of Hot-Electron

Pressure in the Vibration Dynamics of Metal Nanoparticles. *Phys. Rev. Lett.* **2000**, *85*, 792−795.
(16) Wang, L.; Nishijima, Y.; Ueno, K.; Misawa, H.; Tamai, N. Near-Ir Vibrational Dynamics of Periodic Gold Single and Pair Nanocuboids. *Appl. Phys. Lett.* **2009**, *95*, 053116.
(17) Dowgiallo, A.-M.; Schwartzberg, A. M.; Knappenberger, K. L. Structure-Dependent Coherent Acoustic Vibrations of Hollow Gold Nanospheres. *Nano Lett.* **2011**, *11*, 3258−3262.
(18) Hartland, G. V. Coherent Excitation of Vibrational Modes in Metallic Nanoparticles. *Annu. Rev. Phys. Chem.* **2006**, *57*, 403−430.
(19) Pelton, M.; Sader, J. E.; Burgin, J.; Liu, M.; Guyot-Sionnest, P.; Gosztola, D. Damping of Acoustic Vibrations in Gold Nanoparticles. *Nat. Nanotechnol.* **2009**, *4*, 492−495.
(20) Chang, W.-S.; Wen, F.; Chakraborty, D.; Su, M.-N.; Zhang, Y.; Shuang, B.; Nordlander, P.; Sader, J. E.; Halas, N. J.; Link, S. Tuning the Acoustic Frequency of a Gold Nanodisk through Its Adhesion Layer. *Nat. Commun.* **2015**, *6*, 7022.
(21) Burgin, J.; Langot, P.; Del Fatti, N.; Vallée, F.; Huang, W.; El-Sayed, M. A. Time-Resolved Investigation of the Acoustic Vibration of a Single Gold Nanoprism Pair. *J. Phys. Chem. C* **2008**, *112*, 11231−11235.
(22) Hu, M.; Wang, X.; Hartland, G. V.; Mulvaney, P.; Juste, J. P.; Sader, J. E. Vibrational Response of Nanorods to Ultrafast Laser Induced Heating: Theoretical and Experimental Analysis. *J. Am. Chem. Soc.* **2003**, *125*, 14925−14933.
(23) Marty, R.; Arbouet, A.; Girard, C.; Mlayah, A.; Paillard, V.; Lin, V. K.; Teo, S. L.; Tripathy, S. Damping of the Acoustic Vibrations of Individual Gold Nanoparticles. *Nano Lett.* **2011**, *11*, 3301−3306.
(24) Zhu, T.; Snaider, J. M.; Yuan, L.; Huang, L. Ultrafast Dynamic Microscopy of Carrier and Exciton Transport. *Annu. Rev. Phys. Chem.* **2019**, *70*, 219−244.
(25) Beane, G.; Devkota, T.; Brown, B. S.; Hartland, G. V. Ultrafast Measurements of the Dynamics of Single Nanostructures: A Review. *Rep. Prog. Phys.* **2019**, *82*, 016401.
(26) Yi, C.; Su, M.-N.; Dongare, P. D.; Chakraborty, D.; Cai, Y.-Y.; Marolf, D. M.; Kress, R. N.; Ostovar, B.; Tauzin, L. J.; Wen, F.; et al. Polycrystallinity of Lithographically Fabricated Plasmonic Nanostructures Dominates Their Acoustic Vibrational Damping. *Nano Lett.* **2018**, *18*, 3494−3501.
(27) Liu, N.; Giesen, F.; Belov, M.; Losby, J.; Moroz, J.; Fraser, A. E.; McKinnon, G.; Clement, T. J.; Sauer, V.; Hiebert, W. K.; et al. Time-Domain Control of Ultrahigh-Frequency Nanomechanical Systems. *Nat. Nanotechnol.* **2008**, *3*, 715−719.
(28) Medeghini, F.; Crut, A.; Gandolfi, M.; Rossella, F.; Maioli, P.; Vallée, F.; Banfi, F.; Del Fatti, N. Controlling the Quality Factor of a Single Acoustic Nanoresonator by Tuning Its Morphology. *Nano Lett.* **2018**, *18*, 5159−5166.
(29) Wang, J.; Yang, Y.; Wang, N.; Yu, K.; Hartland, G. V.; Wang, G. P. Long Lifetime and Coupling of Acoustic Vibrations of Gold Nanoplates on Unsupported Thin Films. *J. Phys. Chem. A* **2019**, *123*, 10339−10346.
(30) Major, T. A.; Crut, A.; Gao, B.; Lo, S. S.; Fatti, N. D.; Vallée, F.; Hartland, G. V. Damping of the Acoustic Vibrations of a Suspended Gold Nanowire in Air and Water Environments. *Phys. Chem. Chem. Phys.* **2013**, *15*, 4169−4176.
(31) Goubet, N.; Yan, C.; Polli, D.; Portalès, H.; Arfaoui, I.; Cerullo, G.; Pileni, M.-P. Modulating Physical Properties of Isolated and Self-Assembled Nanocrystals through Change in Nanocrystallinity. *Nano Lett.* **2013**, *13*, 504−508.
(32) Portales, H.; Goubet, N.; Saviot, L.; Adichtchev, S.; Murray, D. B.; Mermet, A.; Duval, E.; Pileni, M. P. Probing Atomic Ordering and Multiple Twinning in Metal Nanocrystals through Their Vibrations. *Proc. Natl. Acad. Sci. U. S. A.* **2008**, *105*, 14784.
(33) Su, M.-N.; Dongare, P. D.; Chakraborty, D.; Zhang, Y.; Yi, C.; Wen, F.; Chang, W.-S.; Nordlander, P.; Sader, J. E.; Halas, N. J.; et al. Optomechanics of Single Aluminum Nanodisks. *Nano Lett.* **2017**, *17*, 2575−2583.
(34) Honda, M.; Kumamoto, Y.; Taguchi, A.; Saito, Y.; Kawata, S. Efficient Uv Photocatalysis Assisted by Densely Distributed Aluminum Nanoparticles. *J. Phys. D: Appl. Phys.* **2015**, *48*, 184006.
(35) Bisio, F.; Gonella, G.; Maidecchi, G.; Buzio, R.; Gerbi, A.; Moroni, R.; Giglia, A.; Canepa, M. Broadband Plasmonic Response of Self-Organized Aluminium Nanowire Arrays. *J. Phys. D: Appl. Phys.* **2015**, *48*, 184003.
(36) Su, M.-N.; Ciccarino, C. J.; Kumar, S.; Dongare, P. D.; Hosseini Jebeli, S. A.; Renard, D.; Zhang, Y.; Ostovar, B.; Chang, W.-S.; Nordlander, P.; et al. Ultrafast Electron Dynamics in Single Aluminum Nanostructures. *Nano Lett.* **2019**, *19*, 3091−3097.
(37) Peckus, D.; Henzie, J.; Tamulevičius, T.; Andrulevičius, M.; Lazauskas, A.; Rajackaitė, E.; Meškinis, Š.; Tamulevičius, S. Ultrafast Relaxation Dynamics of Aluminum Nanoparticles in Solution. *Phys. E (Amsterdam, Neth.)* **2020**, *117*, 113795.
(38) Mokkath, J. H.; Henzie, J. One-Dimensional Aluminum Nanoparticle Chains: The Influence of Interparticle Spacing and Chain Length on Plasmon Coupling Behavior. *J. Mater. Chem. C* **2017**, *5*, 4379−4383.
(39) Knight, M. W.; King, N. S.; Liu, L.; Everitt, H. O.; Nordlander, P.; Halas, N. J. Aluminum for Plasmonics. *ACS Nano* **2014**, *8*, 834−840.
(40) Langhammer, C.; Schwind, M.; Kasemo, B.; Zorić, I. Localized Surface Plasmon Resonances in Aluminum Nanodisks. *Nano Lett.* **2008**, *8*, 1461−1471.
(41) Castro-Lopez, M.; Brinks, D.; Sapienza, R.; van Hulst, N. F. Aluminum for Nonlinear Plasmonics: Resonance-Driven Polarized Luminescence of Al, Ag, and Au Nanoantennas. *Nano Lett.* **2011**, *11*, 4674−4678.
(42) Smith, K. J.; Cheng, Y.; Arinze, E. S.; Kim, N. E.; Bragg, A. E.; Thon, S. M. Dynamics of Energy Transfer in Large Plasmonic Aluminum Nanoparticles. *ACS Photonics* **2018**, *5*, 805−813.
(43) McClain, M. J.; Schlather, A. E.; Ringe, E.; King, N. S.; Liu, L.; Manjavacas, A.; Knight, M. W.; Kumar, I.; Whitmire, K. H.; Everitt, H. O.; et al. Aluminum Nanocrystals. *Nano Lett.* **2015**, *15*, 2751−2755.
(44) Lu, S.; Yu, H.; Gottheim, S.; Gao, H.; DeSantis, C. J.; Clark, B. D.; Yang, J.; Jacobson, C. R.; Lu, Z.; Nordlander, P.; et al. Polymer-Directed Growth of Plasmonic Aluminum Nanocrystals. *J. Am. Chem. Soc.* **2018**, *140*, 15412−15418.
(45) Suzaki, Y.; Tachibana, A. Measurement of the Mm Sized Radius of Gaussian Laser Beam Using the Scanning Knife-Edge. *Appl. Opt.* **1975**, *14*, 2809−2810.
(46) Siegman, A. E.; Sasnett, M. W.; Johnston, T. F. Choice of Clip Levels for Beam Width Measurements Using Knife-Edge Techniques. *IEEE J. Quantum Electron.* **1991**, *27*, 1098−1104.
(47) Olson, J.; Dominguez-Medina, S.; Hoggard, A.; Wang, L.-Y.; Chang, W.-S.; Link, S. Optical Characterization of Single Plasmonic Nanoparticles. *Chem. Soc. Rev.* **2015**, *44*, 40−57.
(48) Sönnichsen, C.; Franzl, T.; Wilk, T.; von Plessen, G.; Feldmann, J.; Wilson, O.; Mulvaney, P. Drastic Reduction of Plasmon Damping in Gold Nanorods. *Phys. Rev. Lett.* **2002**, *88*, 077402.
(49) Schultz, S.; Smith, D. R.; Mock, J. J.; Schultz, D. A. Single-Target Molecule Detection with Nonbleaching Multicolor Optical Immunolabels. *Proc. Natl. Acad. Sci. U. S. A.* **2000**, *97*, 996.
(50) Nehl, C. L.; Grady, N. K.; Goodrich, G. P.; Tam, F.; Halas, N. J.; Hafner, J. H. Scattering Spectra of Single Gold Nanoshells. *Nano Lett.* **2004**, *4*, 2355−2359.
(51) Sönnichsen, C.; Alivisatos, A. P. Gold Nanorods as Novel Nonbleaching Plasmon-Based Orientation Sensors for Polarized Single-Particle Microscopy. *Nano Lett.* **2005**, *5*, 301−304.
(52) Novo, C.; Gomez, D.; Perez-Juste, J.; Zhang, Z.; Petrova, H.; Reismann, M.; Mulvaney, P.; Hartland, G. V. Contributions from Radiation Damping and Surface Scattering to the Linewidth of the Longitudinal Plasmon Band of Gold Nanorods: A Single Particle Study. *Phys. Chem. Chem. Phys.* **2006**, *8*, 3540−3546.
(53) Voisin, C.; Del Fatti, N.; Christofilos, D.; Vallée, F. Ultrafast Electron Dynamics and Optical Nonlinearities in Metal Nanoparticles. *J. Phys. Chem. B* **2001**, *105*, 2264−2280.

https://dx.doi.org/10.1021/acs.jpca.0c01190
J. Phys. Chem. A 2020, 124, 3924−3934

(54) Arbouet, A.; Voisin, C.; Christofilos, D.; Langot, P.; Fatti, N. D.; Vallée, F.; Lermé, J.; Celep, G.; Cottancin, E.; Gaudry, M.; et al. Electron-Phonon Scattering in Metal Clusters. *Phys. Rev. Lett.* **2003**, *90*, 177401.
(55) Feldstein, M. J.; Keating, C. D.; Liau, Y.-H.; Natan, M. J.; Scherer, N. F. Electronic Relaxation Dynamics in Coupled Metal Nanoparticles. *J. Am. Chem. Soc.* **1997**, *119*, 6638−6647.
(56) Hodak, J. H.; Henglein, A.; Hartland, G. V. Electron-Phonon Coupling Dynamics in Very Small (between 2 and 8 Nm Diameter) Au Nanoparticles. *J. Chem. Phys.* **2000**, *112*, 5942−5947.
(57) Hodak, J.; Martini, I.; Hartland, G. V. Ultrafast Study of Electron−Phonon Coupling in Colloidal Gold Particles. *Chem. Phys. Lett.* **1998**, *284*, 135−141.
(58) Brorson, S. D.; Fujimoto, J. G.; Ippen, E. P. Femtosecond Electronic Heat-Transport Dynamics in Thin Gold Films. *Phys. Rev. Lett.* **1987**, *59*, 1962−1965.
(59) Link, S.; El-Sayed, M. A. Spectral Properties and Relaxation Dynamics of Surface Plasmon Electronic Oscillations in Gold and Silver Nanodots and Nanorods. *J. Phys. Chem. B* **1999**, *103*, 8410−8426.
(60) Jain, P. K.; Qian, W.; El-Sayed, M. A. Ultrafast Electron Relaxation Dynamics in Coupled Metal Nanoparticles in Aggregates. *J. Phys. Chem. B* **2006**, *110*, 136−142.
(61) Muskens, O. L.; Del Fatti, N.; Vallée, F. Femtosecond Response of a Single Metal Nanoparticle. *Nano Lett.* **2006**, *6*, 552−556.
(62) Lamb, H. On the Vibrations of an Elastic Sphere. *Proc. London Math. Soc.* **1881**, *13*, 189−212.
(63) Tamura, A.; Higeta, K.; Ichinokawa, T. Natural Vibrations of a Spherical Inhomogeneity in an Elastic Medium. *Phys. Solid Earth* **1981**, *17*, 494−504.
(64) Tamura, A.; Higeta, K.; Ichinokawa, T. Lattice Vibrations and Specific Heat of a Small Particle. *J. Phys. C: Solid State Phys.* **1982**, *15*, 4975−4991.
(65) Simmons, G.; Wang, H. *Single Crystal Elastic Constants and Calculated Aggregate Properties: A Handbook*; M.I.T. Press: Cambridge, MA, 1971.
(66) Hu, M.; Hillyard, P.; Hartland, G. V.; Kosel, T.; Perez-Juste, J.; Mulvaney, P. Determination of the Elastic Constants of Gold Nanorods Produced by Seed Mediated Growth. *Nano Lett.* **2004**, *4*, 2493−2497.
(67) Sader, J. E.; Hartland, G. V.; Mulvaney, P. Theory of Acoustic Breathing Modes of Core−Shell Nanoparticles. *J. Phys. Chem. B* **2002**, *106*, 1399−1402.
(68) Crut, A.; Maioli, P.; Fatti, N. D.; Vallée, F. Anisotropy Effects on the Time-Resolved Spectroscopy of the Acoustic Vibrations of Nanoobjects. *Phys. Chem. Chem. Phys.* **2009**, *11*, 5882−5888.
(69) Polli, D.; Lisiecki, I.; Portalès, H.; Cerullo, G.; Pileni, M.-P. Low Sensitivity of Acoustic Breathing Mode Frequency in Co Nanocrystals Upon Change in Nanocrystallinity. *ACS Nano* **2011**, *5*, 5785−5791.
(70) Del Fatti, N.; Voisin, C.; Chevy, F.; Vallée, F.; Flytzanis, C. Coherent Acoustic Mode Oscillation and Damping in Silver Nanoparticles. *J. Chem. Phys.* **1999**, *110*, 11484−11487.
(71) Marks, L. D. Modified Wulff Constructions for Twinned Particles. *J. Cryst. Growth* **1983**, *61*, 556−566.
(72) Xia, Y.; Xiong, Y.; Lim, B.; Skrabalak, S. E. Shape-Controlled Synthesis of Metal Nanocrystals: Simple Chemistry Meets Complex Physics? *Angew. Chem., Int. Ed.* **2009**, *48*, 60−103.
(73) Tinguely, J.-C.; Sow, I.; Leiner, C.; Grand, J.; Hohenau, A.; Felidj, N.; Aubard, J.; Krenn, J. R. Gold Nanoparticles for Plasmonic Biosensing: The Role of Metal Crystallinity and Nanoscale Roughness. *J. Bionanosci.* **2011**, *1*, 128−135.
(74) Tauzin, L. J.; Cai, Y.-Y.; Smith, K. W.; Hosseini Jebeli, S. A.; Bhattacharjee, U.; Chang, W.-S.; Link, S. Exploring the Relationship between Plasmon Damping and Luminescence in Lithographically Prepared Gold Nanorods. *ACS Photonics* **2018**, *5*, 3541−3549.
(75) Devkota, T.; Brown, B. S.; Beane, G.; Yu, K.; Hartland, G. V. Making Waves: Radiation Damping in Metallic Nanostructures. *J. Chem. Phys.* **2019**, *151*, 080901.
(76) Clark, B. D.; DeSantis, C. J.; Wu, G.; Renard, D.; McClain, M. J.; Bursi, L.; Tsai, A.-L.; Nordlander, P.; Halas, N. J. Ligand-Dependent Colloidal Stability Controls the Growth of Aluminum Nanocrystals. *J. Am. Chem. Soc.* **2019**, *141*, 1716−1724.
(77) Hodak, J. H.; Henglein, A.; Hartland, G. V. Size Dependent Properties of Au Particles: Coherent Excitation and Dephasing of Acoustic Vibrational Modes. *J. Chem. Phys.* **1999**, *111*, 8613−8621.
(78) Bonacina, L.; Callegari, A.; Bonati, C.; van Mourik, F.; Chergui, M. Time-Resolved Photodynamics of Triangular-Shaped Silver Nanoplates. *Nano Lett.* **2006**, *6*, 7−10.
(79) Wu, J.; Xiang, D.; Hajisalem, G.; Lin, F.-C.; Huang, J.-S.; Kuo, C.-H.; Gordon, R. Probing the Acoustic Vibrations of Complex-Shaped Metal Nanoparticles with Four-Wave Mixing. *Opt. Express* **2016**, *24*, 23747−23754.
(80) Ruijgrok, P. V.; Zijlstra, P.; Tchebotareva, A. L.; Orrit, M. Damping of Acoustic Vibrations of Single Gold Nanoparticles Optically Trapped in Water. *Nano Lett.* **2012**, *12*, 1063−1069.
(81) Yu, K.; Zijlstra, P.; Sader, J. E.; Xu, Q.-H.; Orrit, M. Damping of Acoustic Vibrations of Immobilized Single Gold Nanorods in Different Environments. *Nano Lett.* **2013**, *13*, 2710−2716.

https://dx.doi.org/10.1021/acs.jpca.0c01190
J. Phys. Chem. A 2020, 124, 3924−3934